Published in final edited form as:
Nature. 2014 September 18; 513(7518): 388–393. doi:10.1038/nature13543.

Molecular architecture and mechanism of the anaphase-promoting complex

Lei-Fu Chang[#1,2,3], **Ziguo Zhang**[#1,2,3], **Jing Yang**[1,2,3], **Stephen H. McLaughlin**[2], and **David Barford**[1,2,3]

[1]Division of Structural Biology, Institute of Cancer Research, 237 Fulham Road, London, SW3 6JB, UK

[2]MRC Laboratory of Molecular Biology, Cambridge, CB2 0QH, UK

[#] These authors contributed equally to this work.

Abstract

The ubiquitination of cell cycle regulatory proteins by the anaphase-promoting complex/cyclosome (APC/C) controls sister chromatid segregation, cytokinesis and the establishment of G1. The APC/C is an unusually large multimeric cullin-RING ligase. Its activity is strictly dependent on regulatory coactivator subunits that promote APC/C – substrate interactions and stimulate its catalytic reaction. Because the structures of many APC/C subunits and their organization within the assembly are unknown, the molecular basis for these processes is poorly understood. Here, from a cryo-EM reconstruction of a human APC/C-coactivator-substrate complex at 7.4 Å resolution, we have determined the complete secondary structural architecture of the complex. With this information we identified protein folds for structurally uncharacterized subunits, and the definitive location of all 20 APC/C subunits within the 1.2 MDa assembly. Comparison with apo APC/C shows that coactivator promotes a profound allosteric transition involving displacement of the cullin-RING catalytic subunits relative to the degron recognition module of coactivator and Apc10. This transition is accompanied by increased flexibility of the cullin-RING subunits and enhanced affinity for UbcH10~ubiquitin, changes which may contribute to coactivator-mediated stimulation of APC/C E3 ligase activity.

Regulation of cell division by reversible protein phosphorylation and ubiquitination involves the coordinated interplay of protein kinases and phosphatases, and ubiquitin ligases and deubiquitinases [1]. The anaphase-promoting complex/cyclosome (APC/C) is an E3 cullin-RING ligase that mediates ubiquitin-dependent proteolysis of specific regulatory proteins to control chromosome segregation in mitosis, the events of cytokinesis and mitotic exit,

Correspondence should be addressed to D.B. (dbarford@mrc-lmb.cam.ac.uk).
[3]Present address: MRC Laboratory of Molecular Biology, Cambridge

Author contributions. L.C. prepared grids, collected and analysed EM data and determined the 3D reconstructions, fitted coordinates and built models, prepared figures and co-wrote the paper. Z.Z. designed and made constructs, performed biochemical analysis and purified proteins. J.Y. prepared and purified the complexes. S.H.McL. performed and analysed SPR experiments. D.B. directed the project, built models and co-wrote the paper.

Author information. EM maps are deposited with the EM-DB with accession codes: 2651 (ternary), 2652 (apo), 2653 (Apc11-ΔRING) and 2654 (ΔApc15).

The authors declare no competing financial interests.

Europe PMC Funders Author Manuscripts

maintenance of G1, and the initiation of DNA replication [2,3]. Through its cullin-RING catalytic module, the APC/C is related to the SCF E3 ligases responsible for controlling S and G2 progression. However, compared to other RING ligases, the APC/C is unusually large. The reasons for its complexity likely arise from its role in orchestrating multiple cell cycle processes, its regulation by protein phosphorylation, and as the ultimate effector of the spindle assembly checkpoint [4].

The activity of the APC/C is tightly controlled by structurally related coactivator subunits (either Cdc20 or Cdh1). Their interaction with the APC/C is reciprocally regulated by CDK-dependent phosphorylation of core APC/C and coactivator subunits, resulting in a switch of Cdc20 and Cdh1 in late mitosis and change of substrate specificity. Coactivators recruit substrates to the APC/C by recognizing conserved destruction motifs or degrons – the D box [5] and KEN box [6]. In addition to their substrate recruitment roles, coactivators stimulate the E3 ligase activity of the APC/C through an unknown mechanism [7].

The activated APC/C-coactivator complex is an assembly of 15 different proteins in vertebrates (~1.2 MDa), of which only four have roles in catalysis (Apc2 and Apc11) and substrate recognition (Apc10 and coactivator) (Extended Data Table 1a). Other large APC/C subunits function as molecular scaffolds to coordinate the juxtaposition of the catalytic and degron-recognition modules, although more direct roles in substrate and/or E2~ubiquitin interactions are also possible. Strikingly, all scaffolding subunits incorporate multiple repeat motifs. These include five TPR (tetratricopeptide repeat) proteins, the PC (proteasome/cyclosome) domain of Apc1, and putative WD40 domain in Apc4.

Reconstitution of recombinant APC/C facilitated its structural and biochemical analysis, providing definition of subunit stoichiometry and the location of many APC/C subunits within the EM-derived molecular envelope [8-10]. However, the structures and locations of numerous APC/C subunits remained unknown, and there were uncertainties regarding the location of its catalytic centre. To address these questions we determined a sub-nanometre resolution EM reconstruction of human APC/C as a ternary complex with the coactivator Cdh1 and a high affinity substrate Hsl1 (refs [11,12]) (APC/C$^{Cdh1.Hsl1}$). From this reconstruction we derived the complete secondary structure of the APC/C allowing us to define the architectures and correctly assign positions of all APC/C subunits. In addition we found that coactivator enhances APC/C affinity for UbcH10~ubiquitin, explaining at least in part how coactivator stimulates APC/C ubiquitination activity. Comparison of ternary and apo APC/C structures defines the basis of the coactivator-mediated allosteric transition and provides insights into the mechanisms underlying this increased affinity for UbcH10.

APC/C architecture

We determined a 3D reconstruction of the human APC/C$^{Cdh1.Hsl1}$ ternary complex to a nominal resolution of 7.4 Å (Fig. 1 and Extended Data Figs 1 and 2 and Table 1b). The resultant map is of sufficient quality to visualize α-helices as discrete rods and β-sheets as planar densities. Figure 1 shows three views of the APC/C with its molecular envelope colour-coded according to subunit assignments, together with the underlying secondary structure elements and architecture of individual APC/C subunits (Supplementary Video 1).

Our higher resolution map indicates revised positions for Apc1 and Apc2. These subunits were previously assigned by means of antibody labelling [13,14] which guided docking of Apc2 into a lower resolution EM map of budding yeast APC/C [15].

The APC/C adopts a triangular shape delineated by a lattice-like shell [8,13-17] (Fig. 1). The back and top of the complex is formed from the bowl-shaped TPR lobe – an assembly of the four canonical TPR proteins and their accessory subunits (Extended Data Table 1a). The base of the APC/C comprises the platform subunits of Apc4 and Apc5, together with two domains of Apc1. Apc1's C-terminal PC domain ($Apc1^{PC}$) extends from the platform to contact the TPR lobe (Fig. 1b, e). The degron-recognition module of Apc10 and Cdh1 is located at the top of the cavity with Apc10 interacting extensively with $Apc1^{PC}$. APC/C's catalytic subunits Apc2 (cullin) and Apc11 (RING) are positioned at the periphery of the platform such that Apc2's C-terminal domain ($Apc2^{CTD}$) and associated Apc11 are at the front of the cavity below Apc10 and Cdh1 (Fig. 1d).

The TPR lobe is a quasi-symmetric array

The four evolutionarily related TPR proteins of the TPR lobe self-associate to form similar V-shaped homo-dimers (Fig. 2a-d). Each subunit comprises an α-helical solenoid with two turns of TPR helix [18-20]. With the N-terminal TPR helix forming the homo-dimer interface, the C-terminal TPR helix creates a protein-binding groove. Apc6 binds its accessory subunit Apc12 through this groove [18,19], whereas the Apc3 and Apc8 homo-dimers utilise one of their dyad-related C-terminal grooves to engage Cdh1 (described below). Apc10 contacts the TPR helical groove of the opposite subunit of the Apc3 homo-dimer. Relative to the full-length *S. pombe* crystal structure [19], Apc6 differs slightly in the context of the APC/C (Extended Data Fig. 3a and 3b and Supplementary Video 1).

TPR homo-dimers stack in parallel to generate a left-handed supra-helix featuring quasi two-fold symmetry (Fig. 1 and Fig. 2e and Supplementary Video 1) [20]. An ordered assembly of the TPR lobe is partly determined by the TPR accessory subunits Apc13 and Apc16 whose extended conformations span multiple TPR subunits (Fig. 2e). Apc16 was identified as a long rod-like density and modelled as a 40-residue α-helix. It lies along the shallow grooves created by α-helices of TPR subunits Apc3 and Apc7 (interfaces i to iii) (Fig. 1 and Extended Data Fig. 3c). The location of Apc16 agrees with its mapping to the upper region of the TPR lobe [21], and its co-purification with an Apc3-Apc7 sub-complex (data not shown). Apc13 interacts with Apc3, Apc6 and Apc8 (interfaces iv to vii) (Fig. 1 and Fig. 2e and Extended Data Fig. 3c), consistent with EM analysis of an Apc13-GFP fusion protein that positioned Apc13 close to the Apc6-Apc3 interface [8].

Architectures of Apc1, Apc4 and Apc5

Apc4 and Apc5 were assigned to the platform through antibody labelling [14], a negative stain EM analysis of an Apc4-Apc5 sub-complex [8], and assignment of toroidal density to the putative WD40 domain of Apc4 (ref. [14]) (Supplementary Video 1). Analysis of the platform in the $APC/C^{Cdh1.Hsl1}$ map reveals that the toroidal density comprises a WD40 domain ($Apc4^{WD40}$) attached to a long helical bundle domain ($Apc4^{HBD}$) (Fig. 3a and Extended Data Fig. 3d). This proposed architecture of Apc4 is consistent with 2D class views of an

Apc4-mFab complex derived using negatively stained electron micrographs (Extended Data Fig. 4), and with secondary structure predictions. Lying alongside Apc4^{HBD} is a TPR helix of 13 TPR motifs (Fig. 1c and Fig. 3b) that corresponds to the TPR domain predicted for Apc5 (Apc5^{TPR}) (ref. [8]). Connected to Apc5^{TPR}, and at one end of Apc4^{HBD}, is a globular domain of nine α-helices (Fig. 1c and Fig. 3b) that we assigned to the predicted N-terminal α-helical domain of Apc5 (Apc5^{NTD}).

Apc1, unambiguously identified from its PC (proteasome-cyclosome) domain (Apc1^{PC}), is located adjacent to Apc2, Apc5 and Apc8 (Fig. 1a, b). Apc1^{PC} resembles the PC domain of the proteasomal subunit Rpn2 (ref. [22]) (Fig. 1a, b and Fig. 3c and Extended Data Fig. 3e). Its eleven PC repeats assemble into a closed toroidal structure of two concentric rings of α-helices encircling two axial α-helices. EM density corresponding to these 24 co-linear α-helices is resolved adjacent to Apc10. The rod-shaped density immediately beneath Apc1^{PC}, connecting it to the platform, resembles an α-helical solenoid (Figs 1b and 3c), and corresponds to the predicted ~300-residue mid-helical domain of Apc1 (Apc1^{MHD}). At the interface of the mid-helical and PC domains, a small β-sandwich structure (Fig. 3c) was assigned to the predicted β-sheet that immediately follows Apc1^{PC}.

A third toroidal-shaped density, located adjacent to Apc1^{MHD}, was assigned as the N-terminal WD40 domain of Apc1 (Apc1^{WD40}) (Fig. 3c and Extended Data Fig. 3f), consistent with the β-strand prediction for the N-terminus of Apc1. Apc1^{WD40} tucks into the helical groove of Apc5^{TPR} (Fig. 1c), and forms an edge-on contact with the C-terminal TPR helix of Apc8B (Fig. 1b).

Apc15 was identified from difference density from a reconstitution of the APC/C with Apc15 deleted (APC/C$^{\Delta Apc15}$) (Fig. 3d and Extended Data Figs 1 and 2). This revealed Apc15 as the helical density bridging Apc8 and Apc5 (Fig. 3e), connected to an extended structure that inserts into the inner groove of the Apc5^{TPR} superhelix (Fig. 3d, e). An interaction of Apc15 with Apc8 and platform subunits is in agreement with biochemical and structural evidence [8,9,23].

The catalytic module is flexible

For Apc2, only α-helices of the N-terminal cullin repeats are clearly identified in the EM map (Fig. 1a, d and Fig. 3f). Density for Apc2^{CTD} and Apc11 is weak and fragmented. In an unsharpened map calculated to reveal low-resolution features, the Apc2^{CTD}-Apc11 module is recovered as a horn-like density (Fig. 3g), similar to a feature described in the 25 Å resolution cryo-EM map of apo *S. pombe* APC/C [16]. 3D classification of the APC/C$^{Cdh1.Hsl1}$ EM data indicated structural variability of this density (Extended Data Fig. 5), consistent with the notion that the Apc2^{CTD}-Apc11 module is flexible. We used a well-defined 3D class to dock Apc2^{CTD}-Apc11, although in this density the Apc11 RING domain cannot be located precisely (Fig. 3g). Because of the flexibility of Apc2^{CTD}, we cannot exclude the possibility that Apc11^{RING} is displaced from Apc2^{CTD}, similar to the Rbx1 RING domain of the activated SCF [24,25].

Degron recognition by Cdh1 and Apc10

Cdh1 and Apc10 are in close proximity within the inner cavity adjacent to the Apc3 homo-dimer [15,17] (Fig. 1a, d and Fig. 4a). We fitted the β-sheets of the WD40 β-propeller domain of Cdh1 (ref. [26]) and the β-sandwich of Apc10 (refs [27,28]) into their respective densities (Fig. 4a and Extended Data Fig. 3h, i). Apc10 and Cdh1 share structurally related C-terminal Ile-Arg motifs (IR tails) that interact with the C-terminal TPR motifs of Apc3 (refs [12,27,29-31]). Density for the IR tails of Cdh1 and Apc10 is visible extending from their globular domains (Fig. 4a). This shows that the two IR tails bind to two equivalent symmetry-related sites in the TPR helices of the Apc3 homo-dimer (Fig. 4b). The three TPR motifs of the IR tail-binding sites were shown previously to be required for IR tail-dependent interactions of Cdh1 to the APC/C [12].

EM density for the Hsl1 substrate is visible at the KEN box-recognition site centred on the upper surface of $Cdh1^{WD40}$ (ref. [26]), whereas D box-assigned density is observed at the D box-coreceptor formed by Cdh1 and Apc10 (refs [15,26,30,32-34]) (Fig. 4a, d). Other segments of Hsl1 are unstructured and not defined in the EM map. Crystallographic studies indicated that the D box-recognition site on coactivator is a channel on the edge of the WD40 domain that engages the D box motif RxxLxx(V/I/L) (residues P1 to P7), but not conserved polar residues P8 to P10 (ref. [26]). In the $APC/C^{Cdh1.Hsl1}$ EM map, we observe tubular density that extends from the D box at the coactivator D box-binding site and connects with Apc10. Modelling this density as P8 to P10 shows that these residues interact with a conserved polar surface on Apc10 (Fig. 4d). Disruption of a loop that comprises this site (the 140s loop) impairs D box-dependent substrate recognition [32]. Ala substitutions of two hydrophilic residues (Ser88 and Asn147) in close proximity to P8 to P10 of the D box (Fig. 4d) attenuates APC/C^{Cdh1} ubiquitination activity, as does mutation of D box residues P8 to P10 (Extended Data Fig. 6). Thus, the D box is a bipartite degron comprising a coactivator-interacting N-terminal [RxxLxx(V/I/L)] motif, and a hydrophilic C-terminal Apc10-binding segment (Fig. 4e).

Cdh1 promotes an allosteric transition

We could also visualize components of the N-terminal segment of Cdh1 ($Cdh1^{NTD}$). This forms a four α-helix bundle that packs co-linearly with the α-helices of $Apc1^{PC}$ and also contacts Apc6 (Fig. 4f, g and Extended Data Fig. 3g). In addition, an extended segment of $Cdh1^{NTD}$ (L1) binds to the inner groove of the Apc8B TPR helix, interacting with three TPR motifs that are structurally related to the IR tail-binding site of Apc3 (Fig. 4c), and which contribute to coactivator binding [12,35].

The N-terminus of coactivator stimulates APC/C ubiquitin ligase activity, independent of degron recognition [7]. To understand coactivator-mediated APC/C activation in the context of our complete subunit assignment, we determined 3D reconstructions of apo APC/C (Extended Data Figs 1 and 2). The most prominent structural difference between apo and ternary complexes involves a displacement of the platform subunits (Fig. 5a, b), similar to those described at lower resolution for *Xenopus* and human APC/C [13,14]. Moreover, in the apo state, EM density for $Apc2^{CTD}$ is more clearly defined (Fig. 5a, c) which, coupled to the

lack of structural variability of Apc2^{CTD} in 3D classes, indicates reduced structural flexibility of Apc2^{CTD} (Extended Data Fig. 7).

Superimposing atomic models of apo and ternary states using Apc1^{PC} and morphing between the two structures, defines the conformational transition induced on coactivator binding (Fig. 5b, d and Supplementary Video 2). This involves a rigid-body rotation of the platform and C-terminal TPR helix of Apc8B around a hinge axis that bisects the Apc1^{PC}-Apc8B interface, propagating a conformational change of 20 Å to the peripheral Apc2^{CTD}-Apc11 catalytic module (Fig. 5b-e and Supplementary Video 2). Driving this rotation is the interaction of Cdh1^{NTD} with Apc1^{PC} and Apc8B. In the apo state, the C-terminal TPR helix of Apc8B is well ordered and interacts with Apc1^{PC} (Fig. 4f). In the ternary complex, Cdh1^{NTD} disrupts this interaction by binding to a site on Apc1^{PC} that overlaps the site in contact with Apc8B. This wedges Apc1^{PC} and Apc8B apart and disorders TPR motifs 13 and 14 of Apc8B (Fig. 4f). A concomitant downwards-displacement of Apc8B tilts the platform to translate the Apc2^{CTD}-Apc11 module upwards (Fig. 5d, e).

Coactivator-induced displacement and flexibility of the Apc2^{CTD}-Apc11 module has implications for understanding how the coactivator NTD stimulates APC/C ubiquitin ligase activity [7]. Increased catalytic activity could result from the flexibility of the Apc2^{CTD}-Apc11 module which, combined with its different location relative to the substrate-recognition module, may provide enhanced substrate (and ubiquitin polymer) access to the APC/C-bound E2~ubiquitin conjugate. Other possibilities include (i) enhancing the affinity of the APC/C for the E2~ubiquitin conjugate, (ii) promoting the closed more reactive configuration of the E2~donor ubiquitin conjugate to stimulate efficient ubiquitin attachment to the target lysine [36-40], or (iii) inducing an allosteric transition of the E2 (ref. [41]).

To assess the effects of Cdh1 on the affinity of APC/C for its cognate E2s we used surface plasmon resonance (SPR). Ternary APC/C bound UbcH10 with a K_d of 0.2 μM, an affinity some three-fold higher than apo APC/C (Fig. 5f and Extended Data Fig. 9). Interestingly, coactivator promoted a more pronounced seven-fold increase in APC/C's affinity for UbcH10~Ub because ubiquitin conjugation of UbcH10 reduced its affinity for apo APC/C nearly three-fold, whereas binding to ternary APC/C was only slightly affected (Fig. 5f and Extended Data Fig. 9). In contrast to UbcH10, ternary and apo APC/C had similar affinities for Ube2S (K_d 0.2 and 0.3 μM) (Fig. 5f and Extended Data Fig. 9), showing that coactivator-mediated APC/C activation does not enhance Ube2S affinity, and consistent with the idea that UbcH10 and Ube2S bind to distinct sites on the complex [40,42]. The C-terminal extension of Ube2S is required for synthesis of poly-ubiquitin chains on APC/C substrates [42-44]. Deleting this C-terminus to yield the UBC domain alone (Ube2S-ΔC) abolished Ube2S binding to the core APC/C [44], a finding we confirmed for both apo and holo APC/C using SPR (Fig. 5f and Extended Data Fig. 9). The Apc2^{CTD}-Apc11 catalytic module had a low affinity for UbcH10 and did not interact with either UbcH10~Ub or Ube2S (Fig. 5f and Extended Data Fig. 9), indicating that high-affinity APC/C interactions with both UbcH10 and Ube2S depend on subunits other than Apc2^{CTD}-Apc11.

That ubiquitin modification of UbcH10 interferes with its binding to apo APC/C suggests that the energetically-favoured conformations of the UbcH10~Ub conjugate, including the catalytically-efficient closed conformation [36-40], are sterically hindered from binding apo APC/C. Thus, in addition to an increased affinity for UbcH10~Ub, a coactivator-dependent conformational change that allows association of UbcH10~Ub in the closed conformation, with enhanced intrinsic catalytic activity, could also contribute to stimulation of APC/C's E3 ligase activity. It is therefore likely that, reminiscent of how Nedd8 conjugation stimulates the SCF [45], multiple mechanisms underlie coactivator-dependent stimulation of the APC/C, and potentially only UbcH10 - responsible for initiating substrate ubiquitination [42,43,46] - is subject to coactivator-mediated regulation.

In conclusion, comparison of our APC/$C^{Cdh1.Hsl1}$ ternary structure with the EM reconstructions of APC/C^{MCC} (ref. [14]) and APC/$C^{Cdh1.Emi1}$ (ref. [47]), determined at lower resolutions, shows that the presence of coactivator in all three complexes is associated with the same activated conformation of the platform subunits (Extended Data Fig. 8a, b). From this analysis it is clear that the MCC makes direct contact with the $Apc2^{CTD}$-Apc11 module, as does the density assigned to the inhibitory zinc-binding region (ZBR) and polybasic tail of Emi1 (ref. [47]), suggesting that these inhibitors may interfere with E2~Ub binding to $Apc2^{CTD}$-Apc11 and/or its flexibility.

A striking feature of the APC/C is the abundance of multiple repeat motif proteins (Extended Data Table 1a). The symmetry of TPR homo-dimers, coupled to the evolution of paralogs, may have resulted in the acquisition of replicated functions. For example, the IR tails of coactivator and Apc10, and NTD of coactivator bind to equivalent sites on three TPR subunits (Fig. 4b, c). Our model of the APC/C provides insights into the assembly of other large multimeric complexes.

Methods

Expression and purification of recombinant human APC/C

Recombinant wild type apo human APC/C and APC/$C^{Cdh1.Hsl1}$ ternary complexes were expressed and purified as described previously [10,20]. We used residues 667 to 872 of Hsl1, a high affinity APC/C^{Cdh1} substrate [11,12]. Apo APC/C with Apc15 deleted (APC/$C^{\Delta Apc15}$) was expressed and purified as for wild type apo human APC/C. To generate APC/C without the Apc11 RING domain (APC/$C^{\Delta RING}$), we inserted a TEV site between Asn19 and Asp20 of Apc11 (APC/$C^{Tev\text{-}RING}$). The resultant complex was purified as for apo APC/C, and the TEV site was cleaved by incubating with TEV protease at 4 °C over night before the final Superpose 6 size exclusion step. This step separated the RING domain from APC/C generating APC/$C^{\Delta RING}$. Mutants of APC/C (APC/$C^{\Delta Apc15}$, APC/$C^{Tev\text{-}RING}$, APC/$C^{Apc10(S88A/N147A)}$) were cloned into the Multibac system [48,49], essentially as described previously [10].

Electron microscopy

Freshly purified recombinant human APC/C in four states (APC/$C^{Cdh1.Hsl1}$ ternary complex, apo APC/C, APC/$C^{\Delta RING}$, and APC/$C^{\Delta Apc15}$) were firstly visualized by negative stain

electron microscopy to check homogeneity. Complexes were then diluted to ~200 μg/ml and aliquots of 2 μl were applied to Quantifoil R1.2/1.3 grids coated with a second layer of home-made thin carbon film, previously glow discharged with the Easiglow discharge unit (Pelco) for 30 s before use. The grids were then blotted for 5 s at room temperature and plunged into liquid ethane using an FEI Vitrobot. Frozen grids were stored in liquid nitrogen. The grids were loaded into a Gatan 626 cryo-holder and transferred to an FEI Tecnai TF20 electron microscope at an accelerating voltage of 200 kV and maintained at approximately −176 °C. The microscope was operated in low-dose mode at a nominal magnification of × 80,000 (~25 $e^{-}/Å^2$). Images were recorded using a Tietz F415 (4k × 4k) CCD camera with a defocus range of ~1.5 μm and ~4 μm and adjacent boxes of 2 × 2 pixels were averaged, resulting in a calibrated sampling of 2.36 Å $pixel^{-1}$. The images were taken manually and only those with a power spectrum showing Thon rings clearly extending beyond 10 Å were selected for further analysis.

Image processing

Particles were selected automatically using the EMAN [50] program *batchboxer* and manually screened with *e2boxer.py* in EMAN2 (ref. [51]). Contrast transfer function parameters were calculated with CTFFING3 (ref. [52]). The coordinates of particles (.box) and the CTFFIND3 log files were imported to RELION [53] to extract the particles, perform 2D and 3D classifications and 3D auto refinement. The negative stain model of the human APC/$C^{Cdh1.Hsl1}$ ternary complex [20] low-pass filtered to 60 Å was used as initial model for refinements of APC/$C^{Cdh1.Hsl1}$ ternary complex and wild type apo state. The resultant map of wild type apo was low-pass filtered to 60 Å and used as an initial model for refinements of APC/$C^{ΔRING}$ and APC/$C^{ΔApc15}$ states. A summary of particles used for refinements is listed in Extended Data Table 1b.

All 3D refinements used gold-standard FSC calculations to avoid overfitting and reported resolutions are based on the FSC = 0.143 criterion [54,55]. Final FSC curves were calculated using a soft spherical mask (with a 5-pixel fall-off) of the two independent reconstructions. To visualize high-resolution details, all density maps were sharpened by applying negative B-factors, estimated using automated procedures (−1200 $Å^2$) [54].

3D classification in RELION was used to examine the heterogeneity of APC/$C^{Cdh1.Hsl1}$ ternary complex, which showed ~60% ternary complex and 40% apo state APC/C. The same approach was also used for classification of the final reconstructions to analyze the flexible parts of the $Apc2^{CTD}$-Apc11 module. For 3D classification, the 3D map refined using all particles was used as reference and local angular searches within 15° were executed. 3D classifications were run for 25 iterations with the following settings: class number =10, angular sampling = 7.5°, and regularization parameter T = 4.

Modelling of APC/C subunits

Modelling of the structures of APC/C subunits combined several approaches. Basically, these can be divided into three categories. (i) Use of available crystal structures of APC/C subunits or their homologous proteins to generate atomic models. This was used for crystal structures of human Apc10 (residues 2-162, PDB code: 1JHJ) [27] and N-terminal seven

helices of Apc7 (residues 21-166, PDB code: 3FFL) [56], *S. pombe* Cut9-Hcn26 complex (Apc6-Apc12 homologue, PDB code: 1XPI) [19], N-terminal dimerization domains of *E. cuniculi* Cdc27 (Apc3 homologue, PDB code: 3KAE) [57] and *S. pombe* Cut23 (Apc8 homologue, PDB code: 3ZN3) [20], and Cdh1-D-KEN (PDB code: 4BH6) [26]. For the C-terminal TPR helices of Apc3, Apc8 and Apc7, the crystal structure of the C-terminal TPR helix of *S. pombe* Cut9 was used as a model. The crystal structure of *S. pombe* Cut9 was also used to build a model of the 13 TPR motifs of Apc5. For Apc2-Apc11, the crystal structure of Cul1 (PDB code: 1U6G) [58] was used as model. For Apc1- PC repeats, structure was predicted with I-Tassar [59] using PC repeats structure of Rpn2 (PDB code: 4ADY) [22] as a reference. (ii) Several domain structures could be recognized directly from our subnanometer resolution maps. For example, the WD40 domain of Cdh1 was used for modelling of Apc4-WD40 and Apc1-WD40 like domains, as seven blades could be seen directly from the EM map. The Apc4-helix-bundle ($Apc4^{HBD}$) was modelled with crystal structure of the four helix-bundle SNARE complex (PDB code: 1SFC) [60]. All these models were rebuilt manually followed by flexible fitting with MDFF. (iii) Small subunits or domains without homologue protein structures were modelled by *ab initio* prediction using Phyre2 (ref. [61]) or substitution with a protein secondary structures (helix, strand or loops). This included Apc13, Apc15, Apc16, N-terminal domain of Apc5 ($Apc5^{NTD}$), mid-helix domain of Apc1 ($Apc1^{MHD}$), Ile-Arg (IR) C-terminal tails of Apc10 and Cdh1, and N-terminal domain of Cdh1 ($Cdh1^{NTD}$).

Fitting atomic coordinates to cryo-EM maps

Rigid-body fitting was performed by ‘fit in map’ program in Chimera [62]. This was applied to Apc10 and the Cdh1 WD40 domain, crystal structure of which fitted well into the cryo EM map without flexible fitting. Flexible fitting for other subunits was performed using MDFF (Molecular dynamics flexible fitting) [63] based on rigid-body fitting. The initial system was prepared for MDFF using Visual Molecular Dynamics (VMD) [64] and run in the Not Another Molecular Dynamics (NAMD) program [65] for 200 ps of simulation time. All MDFF runs were performed with default parameters, using implicit solvent and temperature annealing. For the IR tails of Cdh1 and Apc10, the models were refined with COOT [66].

Map visualization

Map segmentation was based on coordinates docking and carried out using ‘color zone’ in Chimera. Figures were generated using Pymol and Chimera. Videos were recorded with Chimera.

APC/C ubiquitination assays

Proteins were purified in 20 mM HEPES (pH 8.0), 150 mM NaCl, 1 mM DTT. The KEN box of $Hsl1^{667-872}$ was mutated to K675A/E676A/N677A. Based on this KEN box mutation, D box wild type ($Hsl1^{667-872/MutKEN}$) and D box mutant (D box residues P8, P9 and P10) ($Hsl1^{667-872/MutKEN/T835A/N836A/S837A}$) substrates were expressed and purified. Human ubiquitin with an N-terminal His_6 tag was purified in *E. coli*. Human UBA1 was expressed and purified using the pGEX6.1 system. Human UbcH10 was expressed and purified using the pET28 expression system. Human Cdh1 with an N-terminal His_6-HA dual

tag was expressed and purified from insect cells. UbcH10 ubiquitination assays were performed as previously described method with minor modification [10]. Immediately after preparation on ice, APC/C and substrate were added to an ubiquitination mix (containing all components except APC/C and substrate) to 10 μl reaction mix (40 mM Tris (pH 7.5), 10 mM $MgCl_2$, 0.6 mM DTT, 5 mM ATP, 150 nM UBA1 (E1), 300 nM UbcH10 (E2), 2 μM Cdh1, 70 μM His_6-ubiquitin, 0.25 mg/ml BSA, 60 nM APC/C, 2 μM substrate). Reaction mixtures were incubated at room temperature (22 °C) and terminated by addition of SDS/PAGE loading buffer at 0, 10, 20 and 30 mins. Reactions were then analysed by SDS/PAGE (8-12% gradient gels) followed by Western blotting with an antibody against His_6-ubiquitin. Ube2S assays were performed similar to UbcH10 except for use of the modified substrate GST-Hsl1(0K)-His_6-ubiquitin (data not shown).

Apc4-mFab generation and purification

Human Apc4 protein was purified as a by-product of *Hs*APC/C expression and purification. The purified *Hs*Apc4 protein was buffer changed into PBS at 1mg/ml. A number of monoclonal antibodies were prepared using standard procedures (OxFabs). ELISA assays identified three mABs, 152A, 25A and 291A that recognise native HsApc4, and 152A can also recognise denatured Apc4. The antibodies were purified using Protein A sepharose (GE Healthcare Life Sciences). mFabs were generated and purified using the Fab preparation Kit (Pierce). The Apc4-mFab complex for negative stain electron microscopy studies (prepared by mixing Apc4 with mFab 152A at a 2:1 ratio) was further separated by Superpose 6 column (GE Healthcare Life Sciences).

Surface plasmon resonance experiments

Human UbcH10 (Ube2C), ΔN-UbcH10 (residues 4-32 deleted), Ube2S and Ube2S-ΔC (residues 1 to 160) fused to Avi-Tev-His_6 tags were prepared and expressed in *E. coli* using the pET28 expression system. UbcH10 was fused to a C-terminal Avi-Tev-His_6 tag (GSA GLNDIFEAQKIEWHE ENLYFQS HHHHHH) (Avi tag underlined) whereas an N-terminal (HHHHHH ENLYFQS GSAGLNDIFEAQKIEWHE) tag was fused to Ube2S. E2s were purified using Ni-NTA chromatography, TEV cleavage and gel filtration and biotinylated *in vitro* using BirA ligase, (expressed from a pET21a vector (Addgene) and purified as described [67] in buffer: 50 mM bicine, pH 8.3, 10 mM ATP, 10 mM Mg acetate, 250 μM D-biotin for 16 h at 22 °C at a ratio of 10:1 E2:BirA. The biotinylated proteins were further purified by size exclusion chromatography. To prepare UbcH10~Ub, the catalytic Cys 114 was mutated to Lys and conjugated with ubiquitin following a published procedure as described for UbcH5 (ref [37]). Specifically, UbcH10(C114K)-Avi (200 μM) was incubated with His_6-tagged ubiquitin (200 μM) at 35 °C for 24 h in a buffer containing 1 μM UBA1, 3 mM ATP, 5 mM $MgCl_2$, 0.8 mM TCEP, 150 mM NaCl, 50 mM Tris pH 9.5. After addition of 20 mM imidazole, the reaction was applied to a Ni-NTA column pre-equilibrated with Ni-NTA binding/washing buffer (50 mM Tris pH 8.0, 150 mM NaCl, 20 mM imidazole). The free UbcH10(C114K)-Avi flowed through, whereas the conjugate and free ubiquitin were eluted with 100 mM imidazole in Ni-NTA binding/washing buffer. The UbcH10~Ub conjugate was separated from free ubiquitin by S75 size exclusion column. Biotinylated UbcH10~Ub was prepared as for UbcH10.

Apc2 (residues 549-822)-Apc11 (Apc2^{CTD}-Apc11 catalytic module) (baculovirus prepared by William Chao and Jun He) was expressed using the insect cell baculovirus system and purified using streptactin chromatography, TEV cleavage and gel filtration chromatography. Ternary and apo APC/C were purified as above with TEV cleavage to remove the StrepII tag.

SPR was performed using a Biacore T200 using streptavidin-coated sensor chips (SA chips GE Healthcare). Both reference control SA and analyte SA chips were equilibrated in SPR buffer (20 mM HEPES pH 8.0, 200 mM NaCl, 0.02% Tween 20, 0.5 mg/ml BSA, 1 mM DTT) at 20 °C. E2s were immobilised onto the analyte SA chips to reach an RU value of ~400. Analytes (APC/C and Apc2^{CTD}-Apc11) were buffer exchanged into SPR buffer by means of Zebra spin desalting columns (Pierce) and then centrifuged at 30 K *g* for 30 min to remove aggregates. SPR runs were performed with analytes injected for 120 s followed by a 600 s dissociation in 1:2 dilution series with initial concentrations of APC/C at 700 to 900 nM and that of Apc2^{CTD}-Apc11 at ~45 μM. Data were fitted using a single site interaction model using KaleidaGraph (Synergy Software) and Prism (GraphPad Software Inc) to determine k_{on}, k_{off} and $K_d^{(kin)}$, and by measuring the equilibrium response (R_{eq}), where appropriate, near the maximum response to determine $K_d^{(eq)}$. Biotinylation of UbcH10 and Ube2S had no effect on APC/C^{Cdh1} E3 ligase activity, determined at concentrations of 0.3 μM UbcH10 and Ube2S (i.e. close to their K_d values, [data not shown]). ΔN-UbcH10 had similar relative affinities for ternary and apo APC/C (data not shown). The activity of ΔN-UbcH10 relative to untagged wild type UbcH10 in an APC/C^{Cdh1} ubiquitination assay was similar to UbcH10, except for the production of higher molecular weight ubiquitinated Hsl1 species (data not shown). A similar increase in higher molecular weight ubiquitinated products (cyclin A and securin) was reported by [68]. In addition to Avi-Biotin-Ube2S-ΔC as a negative control, a biotinylated peptide corresponding to the biotinylated tag fused to UbcH10 [GSAGLNDIFEAQ(K-Biotin)IEWHEENLYFQ] (Designer BioScience, Cambridge) was immobilized to the analyte SA sensor chip at a similar concentration to the E2s. No interaction with either apo or ternary APC/C was detected (data not shown).

Extended Data

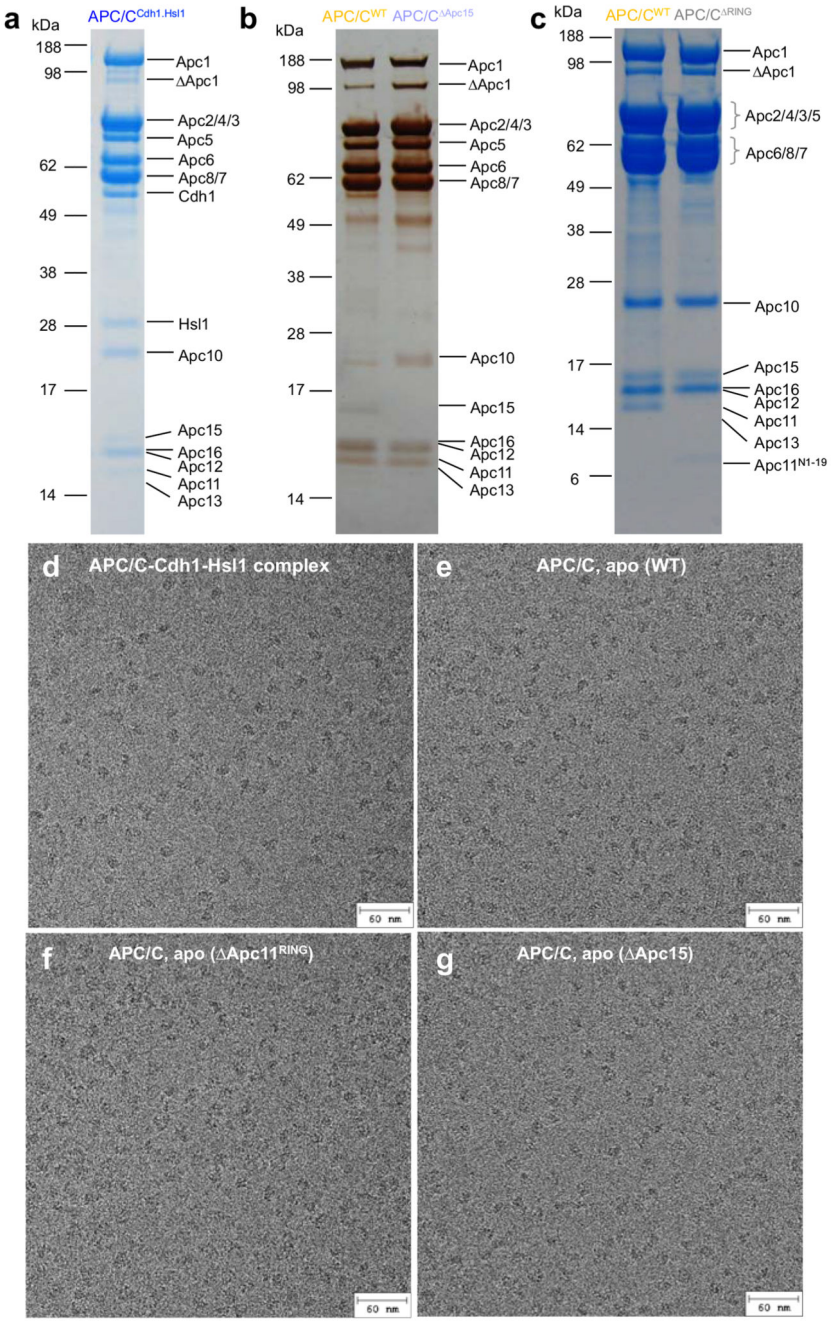

Extended Data Figure 1. APC/C complexes used in this study

(**a**) Coomassie blue stained SDS gel of the human APC/C$^{Cdh1.Hsl1}$ ternary complex. (**b**) Silver stained SDS gel of apo APC/C and APC/C$^{\Delta Apc15}$. (**c**) Coomassie blue stained SDS gel of apo APC/C and APC/C$^{\Delta RING}$. (**d**) Cryo-EM micrograph of APC/C$^{Cdh1.Hsl1}$ ternary complex. (**e**) Cryo-EM micrograph of apo APC/C (WT), (f) cryo-EM micrograph of APC/C$^{\Delta RING}$. (**g**) Cryo-EM micrograph of APC/C$^{\Delta Apc15}$.

Europe PMC Funders Author Manuscripts

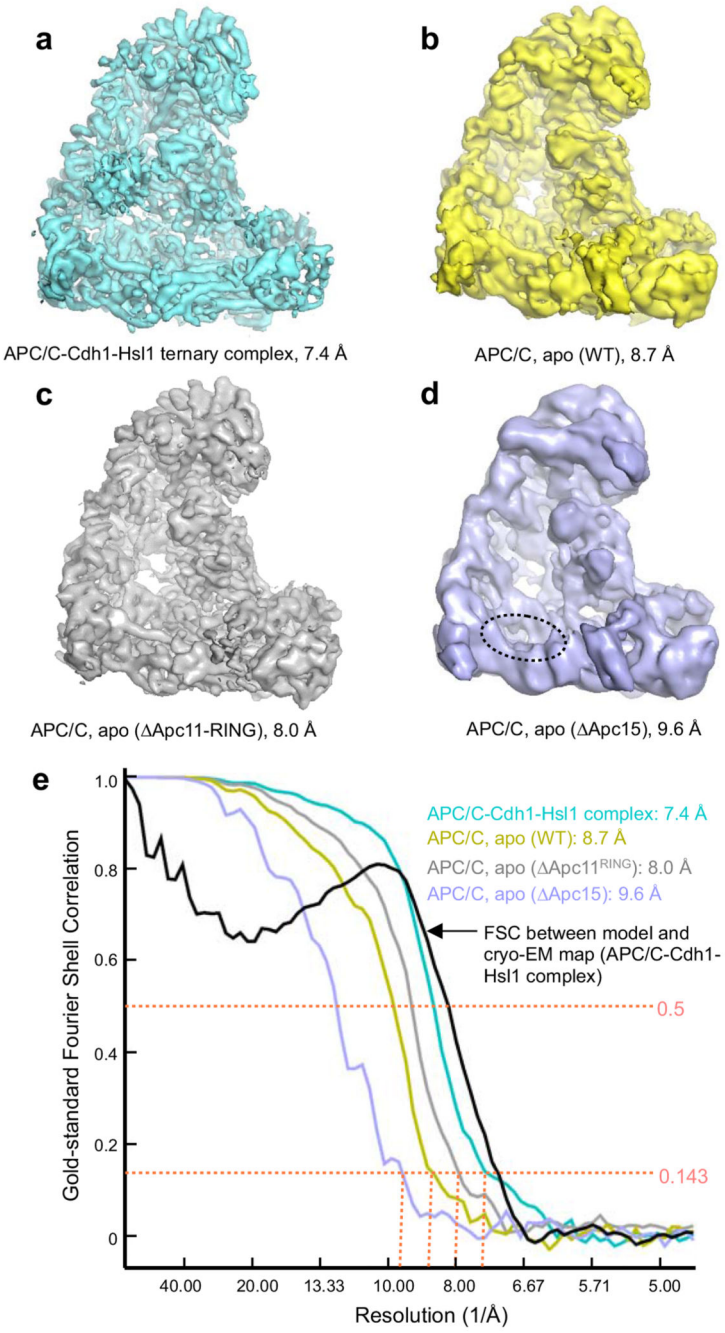

Extended Data Figure 2. EM reconstructions of APC/C complexes described in this study

(a) Human APC/C$^{Cdh1.Hsl1}$ ternary complex. (**b**) Apo APC/C. (**c**) APC/C$^{\Delta RING}$. (**d**) APC/C$^{\Delta Apc15}$. (**e**) Fourier shell correlation (FSC) plots for four complexes. The resolution is based on the 'Gold Standard' criterion of an FSC at 0.143 (refs [54,55]). Also shown is the FSC plot between the atomic model and cryo EM map of APC/C$^{Cdh1.Hsl1}$.

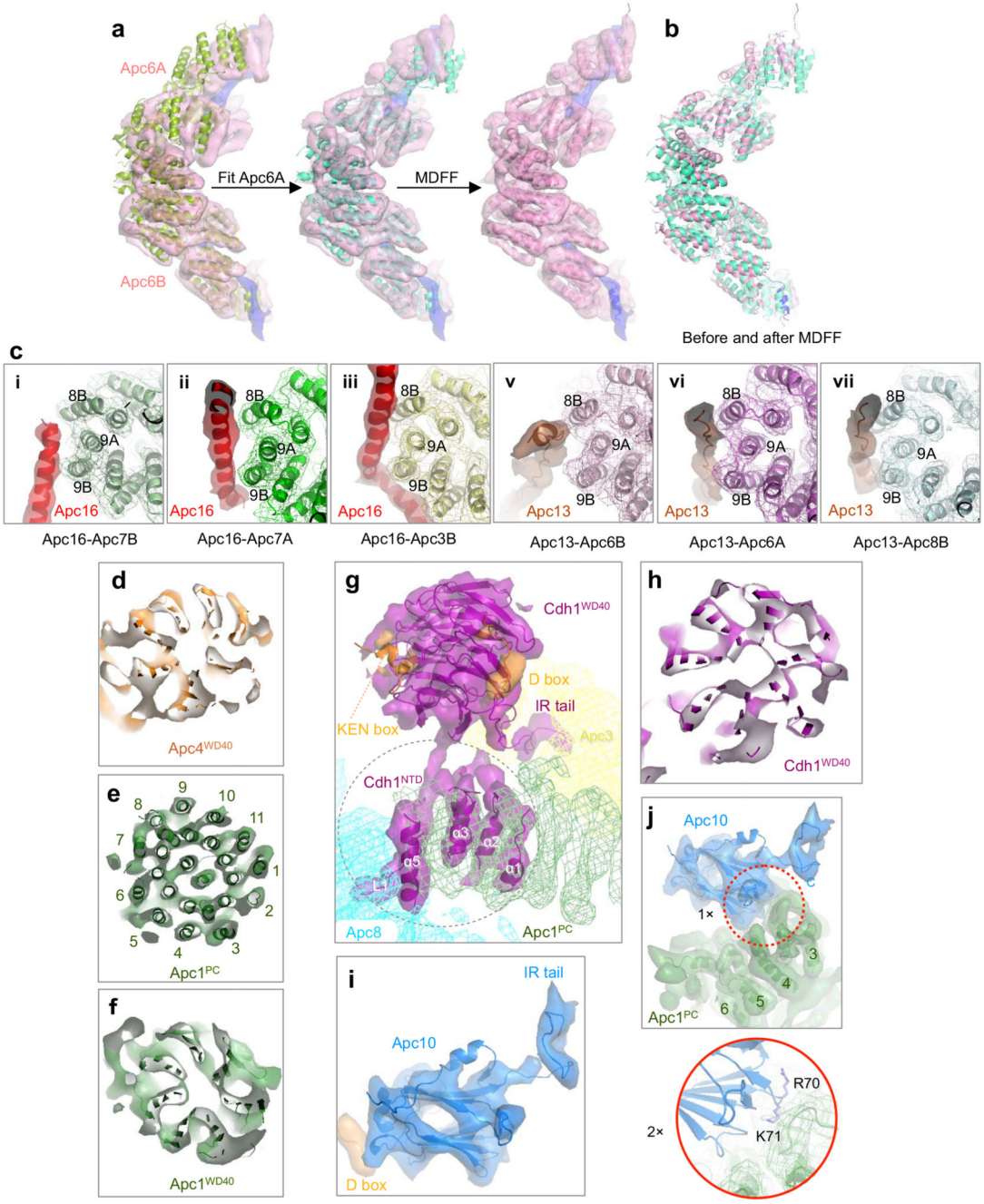

Extended Data Figure 3. Structures of Apc6, Cdh1 and Apc10

(a) Figure to show fitting of *S. pombe* Apc6-Apc12 (Cut9-Hcn26) crystal structure [19] into the segmented Apc6 EM density of APC/$C^{Cdh1.Hsl1}$. (**b**) Superimposition of Apc6-Apc12 before (cyan) and after fitting using MDFF (pink). (**c**) Apc13 and Apc16 interact with structurally equivalent sites (i) to (vii) on seven TPR subunits created by the TPR α-helices 8B, 9A and 9B. Shown are six sites (i) to (iii) (Apc16) and (v) to (vii) (Apc13). Roman numerals refer to interfaces labelled in Fig. 3e. (**d**) Details of $Apc4^{WD40}$, (**i**) $Apc1^{PC}$, (**f**) $Apc1^{WD40}$. (**g**) EM density for Cdh1, (**h**) $Cdh1^{WD40}$ domain, (**i**) Apc10. (**j**) Apc10

interactions with Apc1^{PC} include the conserved 70s loop shown previously to mediate Apc10 association with the APC/C [32].

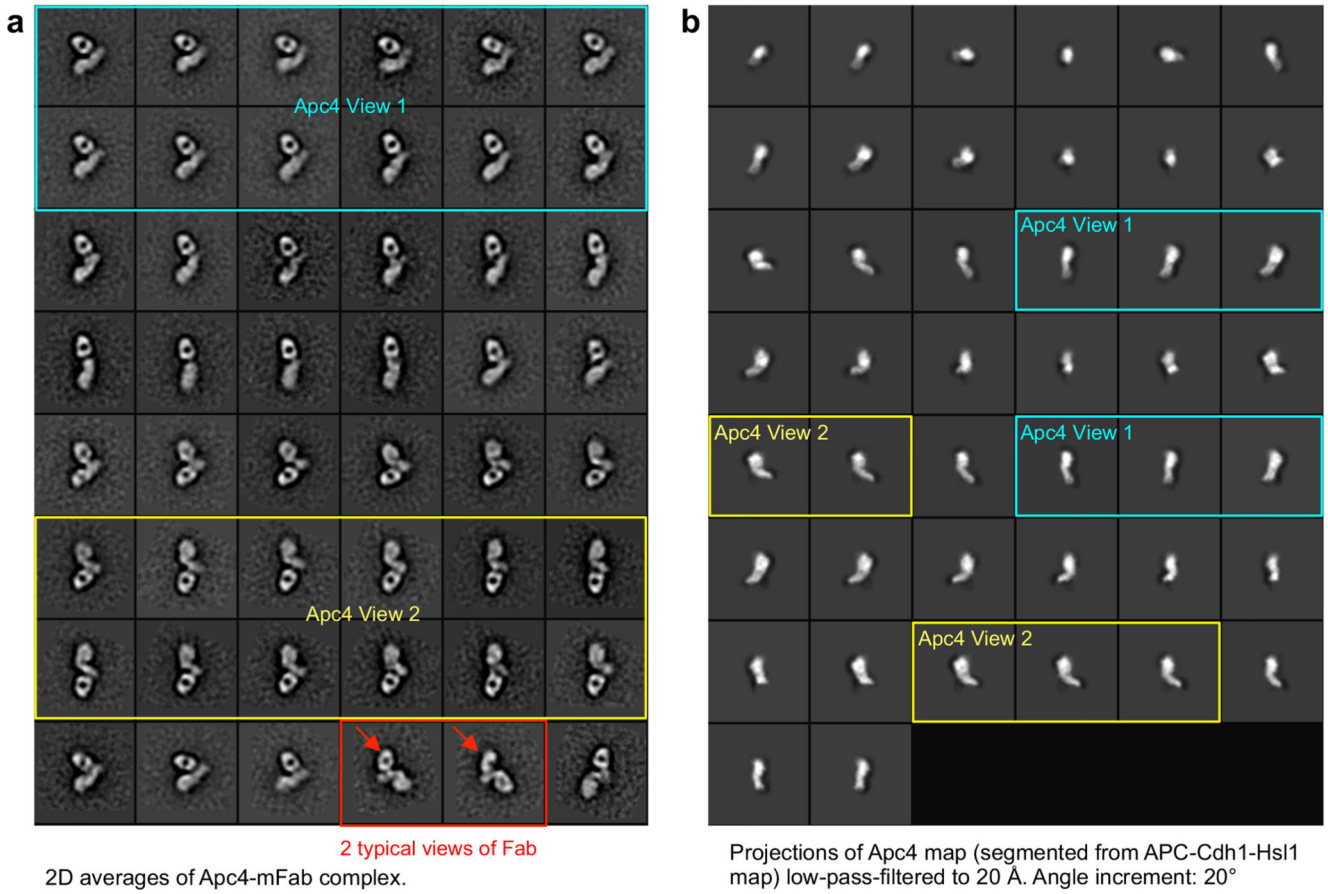

Extended Data Figure 4. Apc-mFab 2D class averages

(a) Selection of 2D class averages derived from negatively stained EM micrographs of Apc4-mFab complexes. Two representative views of mFab are indicated by red arrows. (**b**) Projections of the Apc4 segmented density from the APC/C$^{Cdh1.Hsl1}$ cryo EM map match experimentally-derived 2D class averages of Apc4.

Europe PMC Funders Author Manuscripts

Europe PMC Funders Author Manuscripts

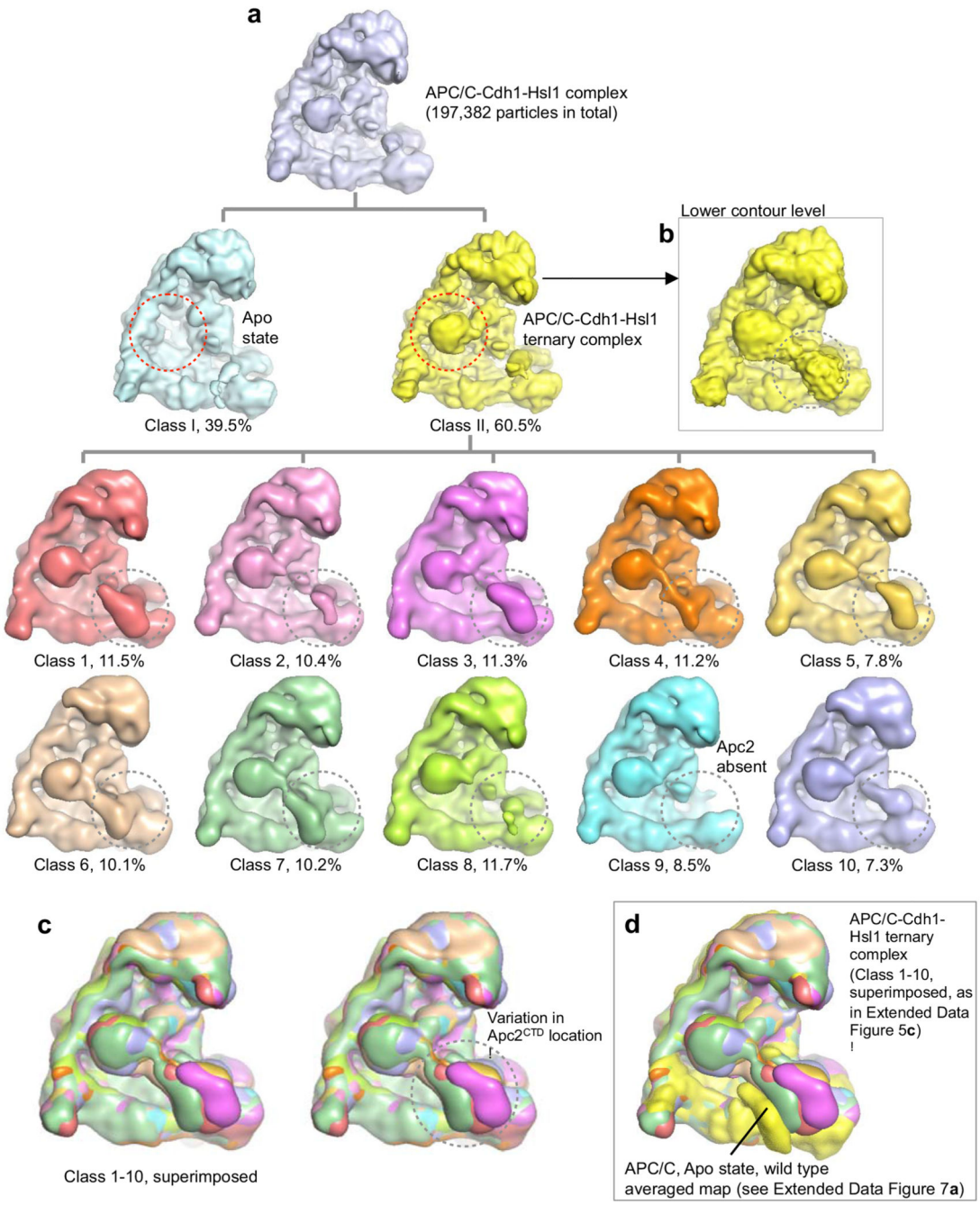

Extended Data Figure 5. 3D classes of APC/C$^{Cd1h.Hsl1}$

(**a**) The major classes were identified showing that the population consisted of 60% ternary complex and 40% apo complex (the Cdh1 position is indicated with a red circle). (**b**) Densities of Apc2^{CTD}-Apc11 are visible only at lower contour level (out-lined by a black circle). Further 3D classification of the ternary complex into 10 classes revealed structural variability of the Apc2^{CTD}-Apc11 module. In one class (Class 9), density for the entire Apc2 is very weak, suggesting loss of this subunit in a small proportion (~8%) of the total**.**

(c) Stereo-view of a superimposition of the 10 3D classes. **(d)** Although variable, Apc2^{CTD}-Apc11 in the ternary complex shifts upward relative to the apo structure (yellow).

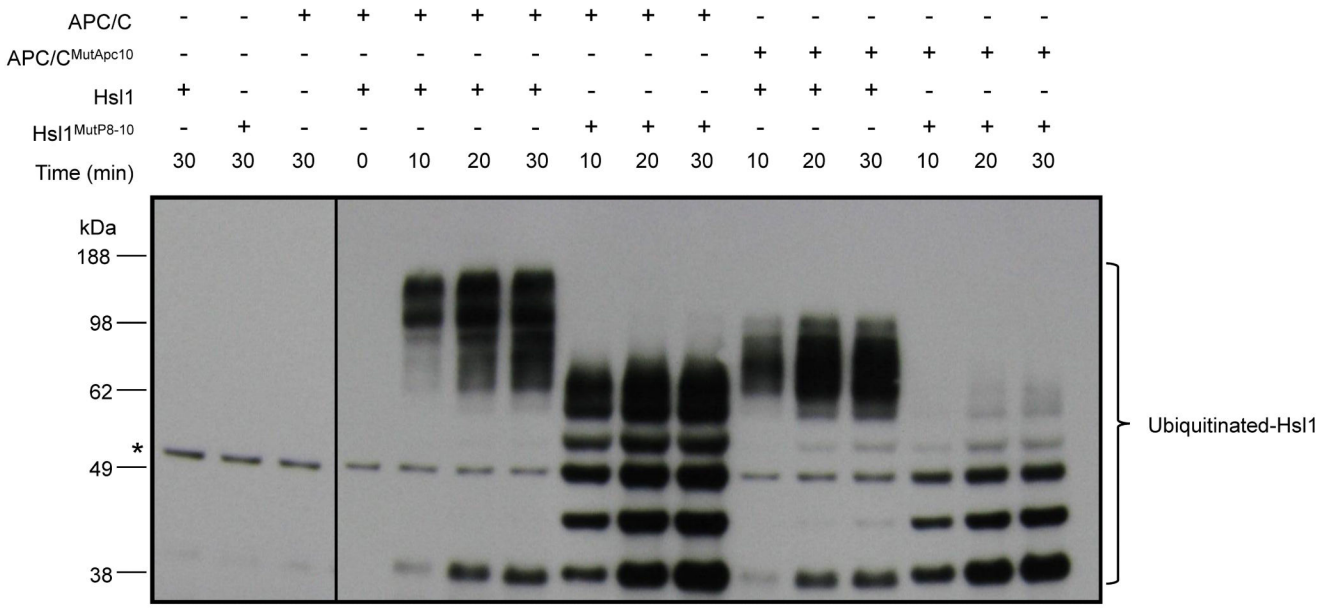

Extended Data Figure 6. APC/C^{Cdh1} ubiquitination of Hsl1 is reduced by Apc10 and D box (P8 to P10) mutations

Mutations of D box residues P8 to P10 to Ala (Hsl1$^{MutP8-10}$) and mutations of Apc10 (S88A/N147A) (APC/C^{MutApc10}) at the D box-binding site reduce APC/C ubiquitination activity. Combining D box and Apc10 mutations potentiated the reduction of APC/C ubiquitination activity. A contaminant band from Uba1 is indicated with an asterisk.

Europe PMC Funders Author Manuscripts

Europe PMC Funders Author Manuscripts

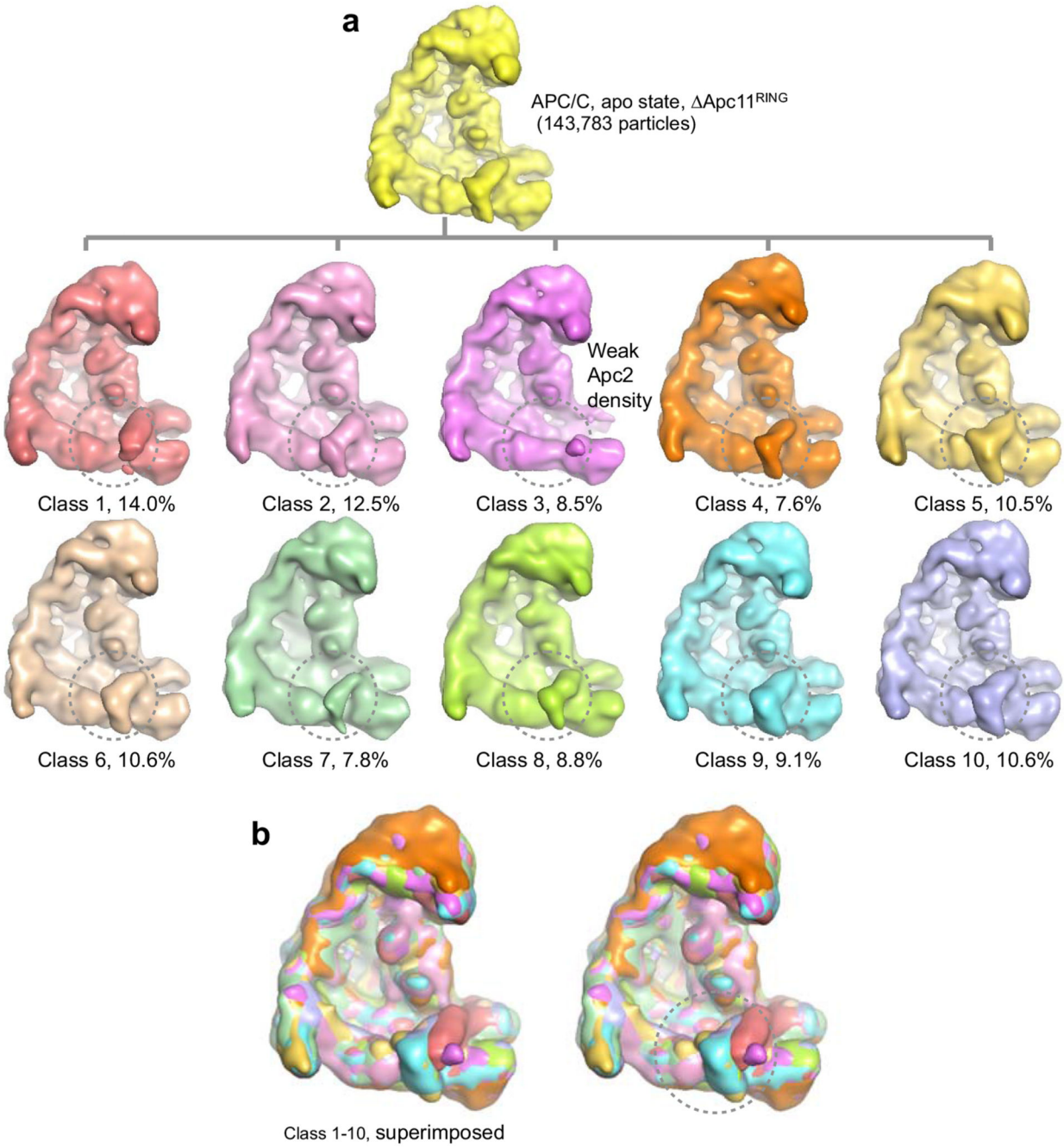

Extended Data Figure 7. 3D classes of apo APC/C

(a) The 10 3D classes of apo APC/C. **(b)** Stereoview of a superimposition of the 10 3D classes shows relatively little structural variability of the Apc2^{CTD}-Apc11 module (circled).

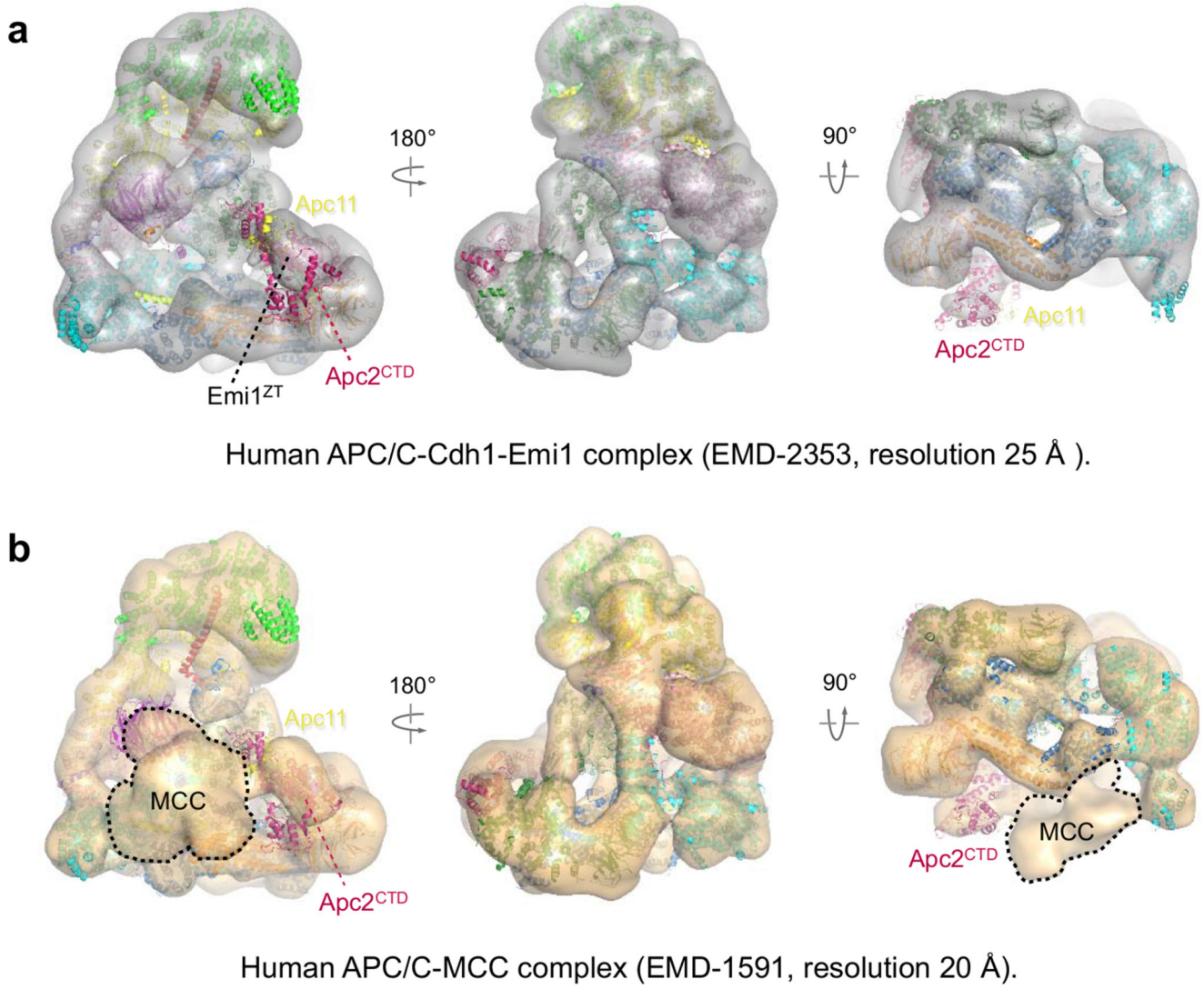

Extended Data Figure 8. Comparison of APC/C$^{Cdh1.Hsl1}$ model with published APC/C EM reconstructions

(a) Human APC/C$^{Cdh1.Emi1}$ (ref. [47]). Density assigned to the inhibitory zinc-binding region and polybasic tail of Emi1 (Emi1^{ZT}) is indicated. (**b**) Human APC/C^{MCC} (ref. [14]). Density corresponding to the mitotic checkpoint complex (MCC) is indicated in a black border. This analysis shows that the activated conformation of APC/C observed in the APC/C$^{Cdh1.Hsl1}$ ternary complex is shared in the inhibited states of APC/C with Emi1 and the MCC (both with coactivator). The Apc2^{CTD}-Apc11 module interacts with MCC and the inhibitory zinc-binding region (ZBR) and C-terminal polybasic tail of Emi1 (Emi1^{ZT}).

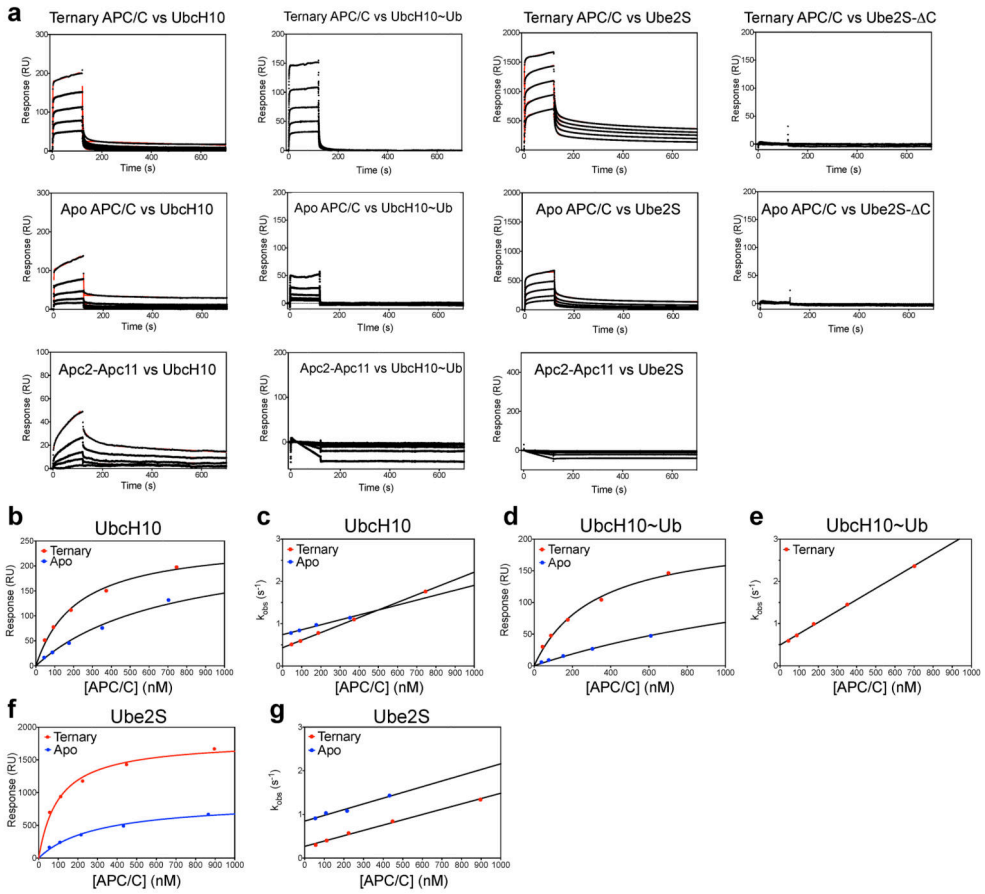

h

Ligand	Analyte	k_{off} (s^{-1})	k_{on} (M^{-1} s^{-1})	K^{eq}_d (nM)	K^{kin}_d (nM)
UbcH10	Ternary APC/C	0.42	1.8 x 10^6	215 ± 32	236 ± 29
	Apo APC/C	0.75	1.1 x 10^6	703 ± 42	682 ± 83
	Apc2^{CTD}-Apc11	0.025	9.9 x 10^2	ND[1]	25,000
UbcH10~Ub	Ternary APC/C	0.40	2.7 x 10^6	318 ± 48	148 ± 9
	Apo APC/C	ND[2]	ND[2]	2,034 ± 57	ND[2]
	Apc2^{CTD}-Apc11	-	-	No binding	No binding
Ube2S	Ternary APC/C	0.18	1.1 x 10^6	230 ± 40	164 ± 17
	Apo APC/C	0.38	1.2 x 10^6	301 ± 50	317 ± 98
	Apc2^{CTD}-Apc11	-	-	No binding	No binding
Ube2SΔC	Ternary APC/C	-	-	No binding	No binding
	Apo APC/C	-	-	No binding	No binding

Extended Data Figure 9. Surface plasmon resonance data

(**a**) SPR sensorgrams for ternary APC/C, apo APC/C and Apc2^{CTD}-Apc11 binding to UbcH10, UbcH10~Ub, Ube2S and Ube2S-ΔC. (**b**) Equilibrium fitting for ternary and apo APC/C association with UbcH10. The equilibrium dissociation constant (K^{eq}_d) is derived from this fit. (**c**) Fit of the observed association rate constant (k_{obs}) ($k_{obs} = k_{on}$[analyte] + k_{off}) for ternary and apo APC/C association with UbcH10. (**d**) Equilibrium fitting for ternary and apo APC/C association with UbcH10~Ub. (**e**) Fit of the observed association rate constant (k_{obs}) for ternary APC/C association with UbcH10~Ub. (**f**). Equilibrium fitting for

Europe PMC Funders Author Manuscripts

ternary and apo APC/C association with Ube2S. The reason for the lower maximum RU at equilibrium for apo APC/C binding to Ube2S, relative to ternary APC/C, is unclear. (**g**) Fit of the observed association rate constant (k_{obs}) (for ternary and apo APC/C association with Ube2S. The rate for 865 nM apo APC/C was not fitted as this was close to the limit of the Biacore T200 response. (**h**) Table summarizing APC/C$^{Cdh1.Hsl1}$ (ternary APC/C), apo APC/C and Apc2^{CTD}-Apc11 dissociation constants for UbcH10, UbcH10~ubiquitin and Ube2S. K^{eq}_d: Equilibrium dissociation constant; K^{kin}_d: kinetic dissociation constant = k_{off}/k_{on}. [1]ND: Not determined because equilibrium binding was not achieved. [2]ND: Not determined due to fast k_{on} and k_{off}. Standard errors of the fit are listed. ΔN-UbcH10 (deletion of residues 4-32 of UbcH10) and UbcH10 had similar relative affinities for ternary and apo APC/C (data not shown).

Extended Data Table 1a
Human APC/C Subunits

Subunit	Mass (kDa)	N	Function	Location	Structural domains
Apc1	216.5	1	Scaffolding	Platform	WD40/mid-helical/PC
Apc4	92.1	1	Scaffolding	Platform	WD40/four helix bundle
Apc5	85.1	1	Scaffolding	Platform	N-terminal helical domain/13 TPR
Apc3	91.9	2	Scaffolding	TPR lobe	14 TPR
Apc6	71.7	2	Scaffolding	TPR lobe	14 TPR
Apc7	66.9	2	Scaffolding	TPR lobe	14 TPR
Apc8	68.8	2	Scaffolding	TPR lobe	14 TPR
Apc12	9.8	2	TPR-accessory	TPR lobe	Extended/α-helix
Apc13	8.5	1	TPR-accessory	TPR lobe	Extended/α-helix
Apc16	11.7	1	TPR-accessory	TPR lobe	α-helix
Apc2	93.8	1	Catalytic	Catalytic module	Cullin repeats/CTD
Apc11	9.8	1	Catalytic	Catalytic module	RING
Apc10	21.2	1	D box recognition	Sub recognition module	Doc homology/IR tail
Apc15	14.3	1	MCC interaction	Platform	Extended/α-helix
Coactivator Cdc20/Cdh1	54.7/55.2	1	D box and KEN box recognition	Sub recognition module	C box/helical/WD40/IR tail
Total APC/C^{Cdh1}	1222.6		-		-

MCC: mitotic checkpoint complex

PC: Proteasome/cyclosome

TPR: Tetratricopeptide repeat

N: stoichiometry

Total mass includes subunit stoichiometry

Extended Data Table 1b
Cryo-EM data used for 3D reconstructions

Samples	Micrographs (N)	Particles all (N)	Particles used (N)	Resolution
APC/C-Cdh1-Hsl1	4,179	197,382	119,386	7.4 Å

Samples	Micrographs (N)	Particles all (N)	Particles used (N)	Resolution
Apo APC/C (WT)	2,696	111,832	111,832	8.7 Å
Apo APC/C (ΔApc15)	1,620	74,935	74,935	9.6 Å
Apo APC/C (ΔApc11-RING)	2.081	143,783	143,783	8.0 Å

Supplementary Material

Refer to Web version on PubMed Central for supplementary material.

Acknowledgments

We thank Paula da Fonseca for her guidance preparing cryo EM grids and Xiaochen Bai and Sjors Scheres for help with the use of RELION and Anna Plechanovova (Dundee) for advice in preparing stable UbcH10~Ub conjugates. We thank David Morgan and William Chao for their comments on the manuscript and David Morgan for communicating data prior to publication. This work was funded by a Cancer Research UK grant to DB.

References

1. Teixeira LK, Reed SI. Ubiquitin ligases and cell cycle control. Annual review of biochemistry. 2013; 82:387–414.
2. Pines J. Cubism and the cell cycle: the many faces of the APC/C. Nat Rev Mol Cell Biol. 2011; 12:427–438. [PubMed: 21633387]
3. Primorac I, Musacchio A. Panta rhei: the APC/C at steady state. The Journal of cell biology. 2013; 201:177–189. [PubMed: 23589490]
4. Lara-Gonzalez P, Westhorpe FG, Taylor SS. The spindle assembly checkpoint. Curr Biol. 2012; 22:R966–980. [PubMed: 23174302]
5. Glotzer M, Murray AW, Kirschner MW. Cyclin is degraded by the ubiquitin pathway. Nature. 1991; 349:132–138. [PubMed: 1846030]
6. Pfleger CM, Kirschner MW. The KEN box: an APC recognition signal distinct from the D box targeted by Cdh1. Genes & development. 2000; 14:655–665. [PubMed: 10733526]
7. Kimata Y, Baxter JE, Fry AM, Yamano H. A role for the Fizzy/Cdc20 family of proteins in activation of the APC/C distinct from substrate recruitment. Molecular cell. 2008; 32:576–583. [PubMed: 19026787]
8. Schreiber A, et al. Structural basis for the subunit assembly of the anaphase-promoting complex. Nature. 2011; 470:227–232. [PubMed: 21307936]
9. Uzunova K, et al. APC15 mediates CDC20 autoubiquitylation by APC/C(MCC) and disassembly of the mitotic checkpoint complex. Nature structural & molecular biology. 2012; 19:1116–1123.
10. Zhang Z, et al. Recombinant expression, reconstitution and structure of human anaphase-promoting complex (APC/C). Biochem J. 2013; 449:365–371. [PubMed: 23078409]
11. Burton JL, Solomon MJ. D box and KEN box motifs in budding yeast Hsl1p are required for APC-mediated degradation and direct binding to Cdc20p and Cdh1p. Genes & development. 2001; 15:2381–2395. [PubMed: 11562348]
12. Matyskiela ME, Morgan DO. Analysis of activator-binding sites on the APC/C supports a cooperative substrate-binding mechanism. Molecular cell. 2009; 34:68–80. [PubMed: 19362536]
13. Dube P, et al. Localization of the coactivator Cdh1 and the cullin subunit Apc2 in a cryo-electron microscopy model of vertebrate APC/C. Molecular cell. 2005; 20:867–879. [PubMed: 16364912]
14. Herzog F, et al. Structure of the anaphase-promoting complex/cyclosome interacting with a mitotic checkpoint complex. Science. 2009; 323:1477–1481. [PubMed: 19286556]
15. da Fonseca PC, et al. Structures of APC/C(Cdh1) with substrates identify Cdh1 and Apc10 as the D-box co-receptor. Nature. 2011; 470:274–278. [PubMed: 21107322]

16. Ohi MD, et al. Structural organization of the anaphase-promoting complex bound to the mitotic activator Slp1. Molecular cell. 2007; 28:871–885. [PubMed: 18082611]
17. Buschhorn BA, et al. Substrate binding on the APC/C occurs between the coactivator Cdh1 and the processivity factor Doc1. Nature structural & molecular biology. 2011; 18:6–13.
18. Wang J, Dye BT, Rajashankar KR, Kurinov I, Schulman BA. Insights into anaphase promoting complex TPR subdomain assembly from a CDC26-APC6 structure. Nature structural & molecular biology. 2009
19. Zhang Z, Kulkarni K, Hanrahan SJ, Thompson AJ, Barford D. The APC/C subunit Cdc16/Cut9 is a contiguous tetratricopeptide repeat superhelix with a homo-dimer interface similar to Cdc27. The EMBO journal. 2010; 29:3733–3744. [PubMed: 20924356]
20. Zhang Z, et al. The four canonical tpr subunits of human APC/C form related homo-dimeric structures and stack in parallel to form a TPR suprahelix. Journal of molecular biology. 2013; 425:4236–4248. [PubMed: 23583778]
21. Hutchins JR, et al. Systematic analysis of human protein complexes identifies chromosome segregation proteins. Science. 2010; 328:593–599. [PubMed: 20360068]
22. He J, et al. The structure of the 26S proteasome subunit Rpn2 reveals its PC repeat domain as a closed toroid of two concentric alpha-helical rings. Structure. 2012; 20:513–521. [PubMed: 22405010]
23. Hall MC, Torres MP, Schroeder GK, Borchers CH. Mnd2 and Swm1 are core subunits of the Saccharomyces cerevisiae anaphase-promoting complex. The Journal of biological chemistry. 2003; 278:16698–16705. [PubMed: 12609981]
24. Duda DM, et al. Structural insights into NEDD8 activation of cullin-RING ligases: conformational control of conjugation. Cell. 2008; 134:995–1006. [PubMed: 18805092]
25. Calabrese MF, et al. A RING E3-substrate complex poised for ubiquitin-like protein transfer: structural insights into cullin-RING ligases. Nature structural & molecular biology. 2011; 18:947–949.
26. He J, et al. Insights into Degron Recognition by APC/C Coactivators from the Structure of an Acm1-Cdh1 Complex. Molecular cell. 2013; 50:649–660. [PubMed: 23707760]
27. Wendt KS, et al. Crystal structure of the APC10/DOC1 subunit of the human anaphase-promoting complex. Nat Struct Biol. 2001; 8:784–788. [PubMed: 11524682]
28. Au SW, Leng X, Harper JW, Barford D. Implications for the ubiquitination reaction of the anaphase-promoting complex from the crystal structure of the Doc1/Apc10 subunit. Journal of molecular biology. 2002; 316:955–968. [PubMed: 11884135]
29. Vodermaier HC, Gieffers C, Maurer-Stroh S, Eisenhaber F, Peters JM. TPR subunits of the anaphase-promoting complex mediate binding to the activator protein CDH1. Curr Biol. 2003; 13:1459–1468. [PubMed: 12956947]
30. Kraft C, Vodermaier HC, Maurer-Stroh S, Eisenhaber F, Peters JM. The WD40 propeller domain of Cdh1 functions as a destruction box receptor for APC/C substrates. Molecular cell. 2005; 18:543–553. [PubMed: 15916961]
31. Thornton BR, et al. An architectural map of the anaphase-promoting complex. Genes & development. 2006; 20:449–460. [PubMed: 16481473]
32. Carroll CW, Enquist-Newman M, Morgan DO. The APC subunit Doc1 promotes recognition of the substrate destruction box. Curr Biol. 2005; 15:11–18. [PubMed: 15649358]
33. Chao WC, Kulkarni K, Zhang Z, Kong EH, Barford D. Structure of the mitotic checkpoint complex. Nature. 2012; 484:208–213. [PubMed: 22437499]
34. Tian W, et al. Structural analysis of human Cdc20 supports multisite degron recognition by APC/C. Proceedings of the National Academy of Sciences of the United States of America. 2012; 109:18419–18424. [PubMed: 23091007]
35. Izawa D, Pines J. How APC/C-Cdc20 changes its substrate specificity in mitosis. Nature cell biology. 2011; 13:223–233.
36. Dou H, Buetow L, Sibbet GJ, Cameron K, Huang DT. BIRC7-E2 ubiquitin conjugate structure reveals the mechanism of ubiquitin transfer by a RING dimer. Nature structural & molecular biology. 2012; 19:876–883.

37. Plechanovova A, Jaffray EG, Tatham MH, Naismith JH, Hay RT. Structure of a RING E3 ligase and ubiquitin-loaded E2 primed for catalysis. Nature. 2012; 489:115–120. [PubMed: 22842904]
38. Pruneda JN, et al. Structure of an E3:E2~Ub complex reveals an allosteric mechanism shared among RING/U-box ligases. Molecular cell. 2012; 47:933–942. [PubMed: 22885007]
39. Saha A, Lewis S, Kleiger G, Kuhlman B, Deshaies RJ. Essential role for ubiquitin-ubiquitin-conjugating enzyme interaction in ubiquitin discharge from Cdc34 to substrate. Molecular cell. 2011; 42:75–83. [PubMed: 21474069]
40. Wickliffe KE, Lorenz S, Wemmer DE, Kuriyan J, Rape M. The mechanism of linkage-specific ubiquitin chain elongation by a single-subunit e2. Cell. 2011; 144:769–781. [PubMed: 21376237]
41. Das R, et al. Allosteric activation of E2-RING finger-mediated ubiquitylation by a structurally defined specific E2-binding region of gp78. Molecular cell. 2009; 34:674–685. [PubMed: 19560420]
42. Williamson A, et al. Identification of a physiological E2 module for the human anaphase-promoting complex. Proceedings of the National Academy of Sciences of the United States of America. 2009; 106:18213–18218. [PubMed: 19822757]
43. Wu T, et al. UBE2S drives elongation of K11-linked ubiquitin chains by the anaphase-promoting complex. Proceedings of the National Academy of Sciences of the United States of America. 2010; 107:1355–1360. [PubMed: 20080579]
44. Wang W, Kirschner MW. Emi1 preferentially inhibits ubiquitin chain elongation by the anaphase-promoting complex. Nature cell biology. 2013; 15:797–806.
45. Saha A, Deshaies RJ. Multimodal activation of the ubiquitin ligase SCF by Nedd8 conjugation. Molecular cell. 2008; 32:21–31. [PubMed: 18851830]
46. Jin L, Williamson A, Banerjee S, Philipp I, Rape M. Mechanism of ubiquitin-chain formation by the human anaphase-promoting complex. Cell. 2008; 133:653–665. [PubMed: 18485873]
47. Frye JJ, et al. Electron microscopy structure of human APC/C(CDH1)-EMI1 reveals multimodal mechanism of E3 ligase shutdown. Nature structural & molecular biology. 2013; 20:827–835.
48. Berger I, Fitzgerald DJ, Richmond TJ. Baculovirus expression system for heterologous multiprotein complexes. Nat Biotechnol. 2004; 22:1583–1587. [PubMed: 15568020]
49. Fitzgerald DJ, et al. Multiprotein expression strategy for structural biology of eukaryotic complexes. Structure. 2007; 15:275–279. [PubMed: 17355863]
50. Ludtke SJ, Baldwin PR, Chiu W. EMAN: semiautomated software for high-resolution single-particle reconstructions. Journal of structural biology. 1999; 128:82–97. [PubMed: 10600563]
51. Tang G, et al. EMAN2: an extensible image processing suite for electron microscopy. Journal of structural biology. 2007; 157:38–46. [PubMed: 16859925]
52. Mindell JA, Grigorieff N. Accurate determination of local defocus and specimen tilt in electron microscopy. Journal of structural biology. 2003; 142:334–347. [PubMed: 12781660]
53. Scheres SH. RELION: implementation of a Bayesian approach to cryo-EM structure determination. Journal of structural biology. 2012; 180:519–530. [PubMed: 23000701]
54. Rosenthal PB, Henderson R. Optimal determination of particle orientation, absolute hand, and contrast loss in single-particle electron cryomicroscopy. Journal of molecular biology. 2003; 333:721–745. [PubMed: 14568533]
55. Scheres SH, Chen S. Prevention of overfitting in cryo-EM structure determination. Nature methods. 2012; 9:853–854. doi:10.1038/nmeth.2115. [PubMed: 22842542]
56. Han D, et al. Crystal structure of the N-terminal domain of anaphase-promoting complex subunit 7. The Journal of biological chemistry. 2009; 284:15137–15146. [PubMed: 19091741]
57. Zhang Z, et al. Molecular structure of the N-terminal domain of the APC/C subunit Cdc27 reveals a homo-dimeric tetratricopeptide repeat architecture. Journal of molecular biology. 2010; 397:1316–1328. [PubMed: 20206185]
58. Zheng N, et al. Structure of the Cul1-Rbx1-Skp1-F boxSkp2 SCF ubiquitin ligase complex. Nature. 2002; 416:703–709. [PubMed: 11961546]
59. Roy A, Kucukural A, Zhang Y. I-TASSER: a unified platform for automated protein structure and function prediction. Nature protocols. 2010; 5:725–738. doi:10.1038/nprot.2010.5.

60. Sutton RB, Fasshauer D, Jahn R, Brunger AT. Crystal structure of a SNARE complex involved in synaptic exocytosis at 2.4 A resolution. Nature. 1998; 395:347–353. [PubMed: 9759724]
61. Kelley LA, Sternberg MJ. Protein structure prediction on the Web: a case study using the Phyre server. Nature protocols. 2009; 4:363–371.
62. Yang Z, et al. UCSF Chimera, MODELLER, and IMP: an integrated modeling system. Journal of structural biology. 2012; 179:269–278. [PubMed: 21963794]
63. Trabuco LG, Villa E, Schreiner E, Harrison CB, Schulten K. Molecular dynamics flexible fitting: a practical guide to combine cryo-electron microscopy and X-ray crystallography. Methods. 2009; 49:174–180. [PubMed: 19398010]
64. Humphrey W, Dalke A, Schulten K. VMD: visual molecular dynamics. Journal of molecular graphics. 1996; 14(33-38):27–38.
65. Phillips JC, et al. Scalable molecular dynamics with NAMD. J Comput Chem. 2005; 26:1781–1802. [PubMed: 16222654]
66. Emsley P, Cowtan K. Coot: model-building tools for molecular graphics. Acta Crystallogr D Biol Crystallogr. 2004; 60:2126–2132. [PubMed: 15572765]
67. Li Y, Sousa R. Expression and purification of E. coli BirA biotin ligase for in vitro biotinylation. Protein expression and purification. 2012; 82:162–167. doi:10.1016/j.pep.2011.12.008. [PubMed: 22227598]
68. Summers MK, Pan B, Mukhyala K, Jackson PK. The unique N terminus of the UbcH10 E2 enzyme controls the threshold for APC activation and enhances checkpoint regulation of the APC. Molecular cell. 2008; 31:544–556. [PubMed: 18722180]

Europe PMC Funders Author Manuscripts

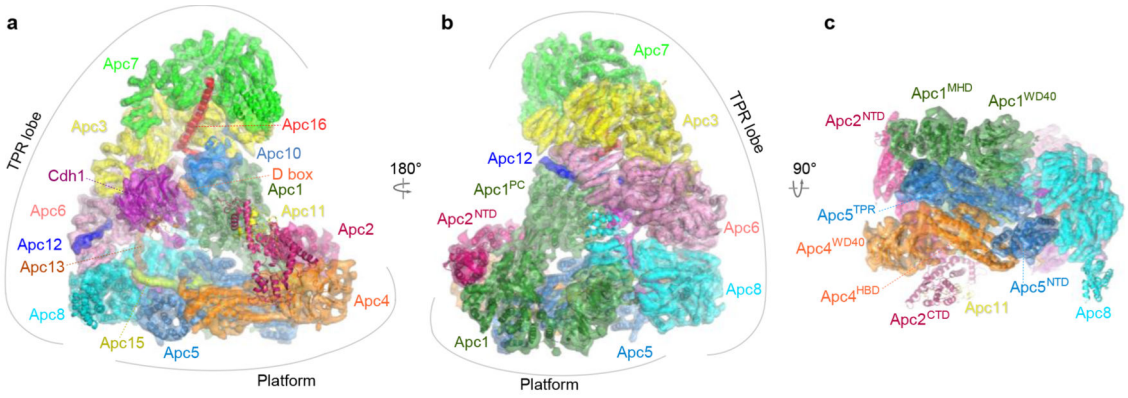

Figure 1. EM reconstructions of the *H. sapiens* APC/C$^{Cdh1.Hsl1}$ ternary complex at 7.4 Å resolution

(**a-c**) Three views of the molecular envelope with the EM map segmented and colour-coded according to subunit assignments. The molecular envelope is represented as a transparent surface to view the underlying secondary structural elements and subunit architectures.

Europe PMC Funders Author Manuscripts

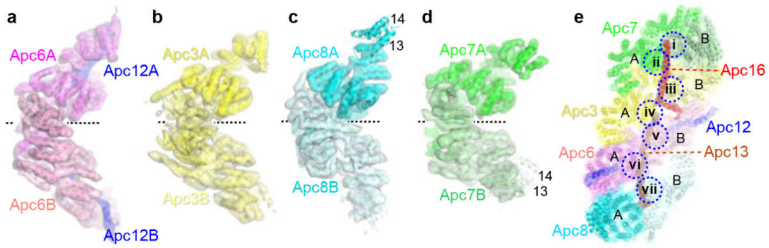

Figure 2. The TPR homo-dimers assemble to form a quasi-symmetric array

(**a**) – (**d**). The four canonical TPR homo-dimers form structurally related 'V'-shaped homo-dimers. Shown are the segmented EM maps and tertiary structures of Apc6, Apc3, Apc8 and Apc7. The two subunits of the homo-dimer are designated 'A' and 'B' and for Apc6 are shown in two shades of magenta. C-terminal TPR motifs 13 and 14 of Apc7B and Apc8A project into solvent and are partially disordered. (**e**). Front view of the TPR lobe showing how the TPR accessory subunits Apc13 and Apc16 span multiple TPR subunits. Roman numerals refer to interfaces indicated in Extended Data Fig. 3c.

Europe PMC Funders Author Manuscripts

Europe PMC Funders Author Manuscripts

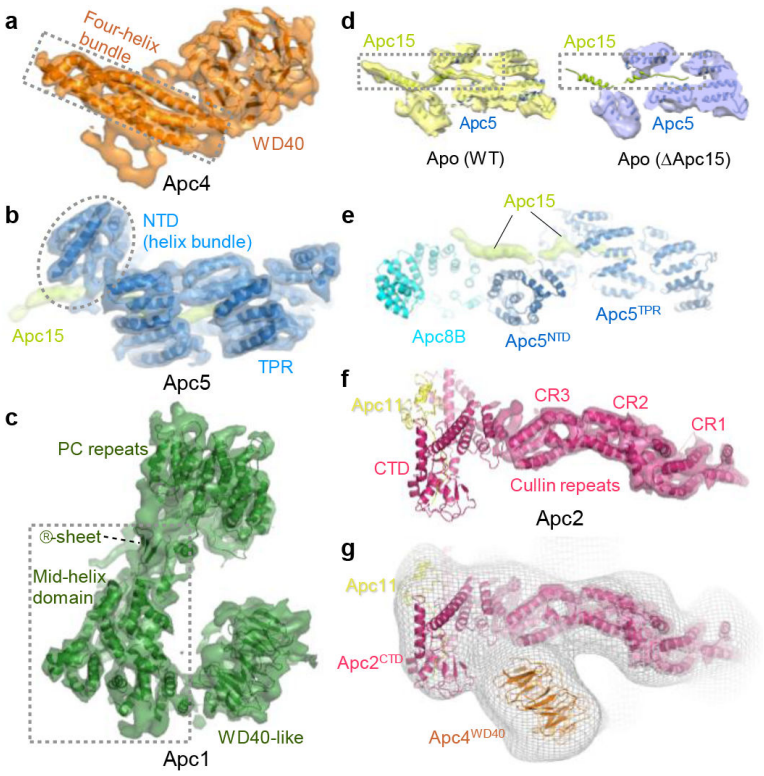

Figure 3. Architecture of platform subunits

(**a**) Overall view of Apc4, (**b**) Apc5 with Apc15, (**c**) Apc1. (**d**) Deletion analysis reveals Apc15 density in the vicinity of Apc5: (left) apo APC/C, (right) apo APC/C$^{\Delta Apc15}$. (**e**) Apc15-assigned density contacts Apc8 and Apc5. (**f**) Only Apc2^{NTD} (cullin repeats) is visible in the sharpened EM map, whereas the flexibility of the Apc2^{CTD}-Apc11 module results in weak fragmented density. (**g**) An unsharpened map from 3D classification indicates the position of the Apc2^{CTD}-Apc11 module.

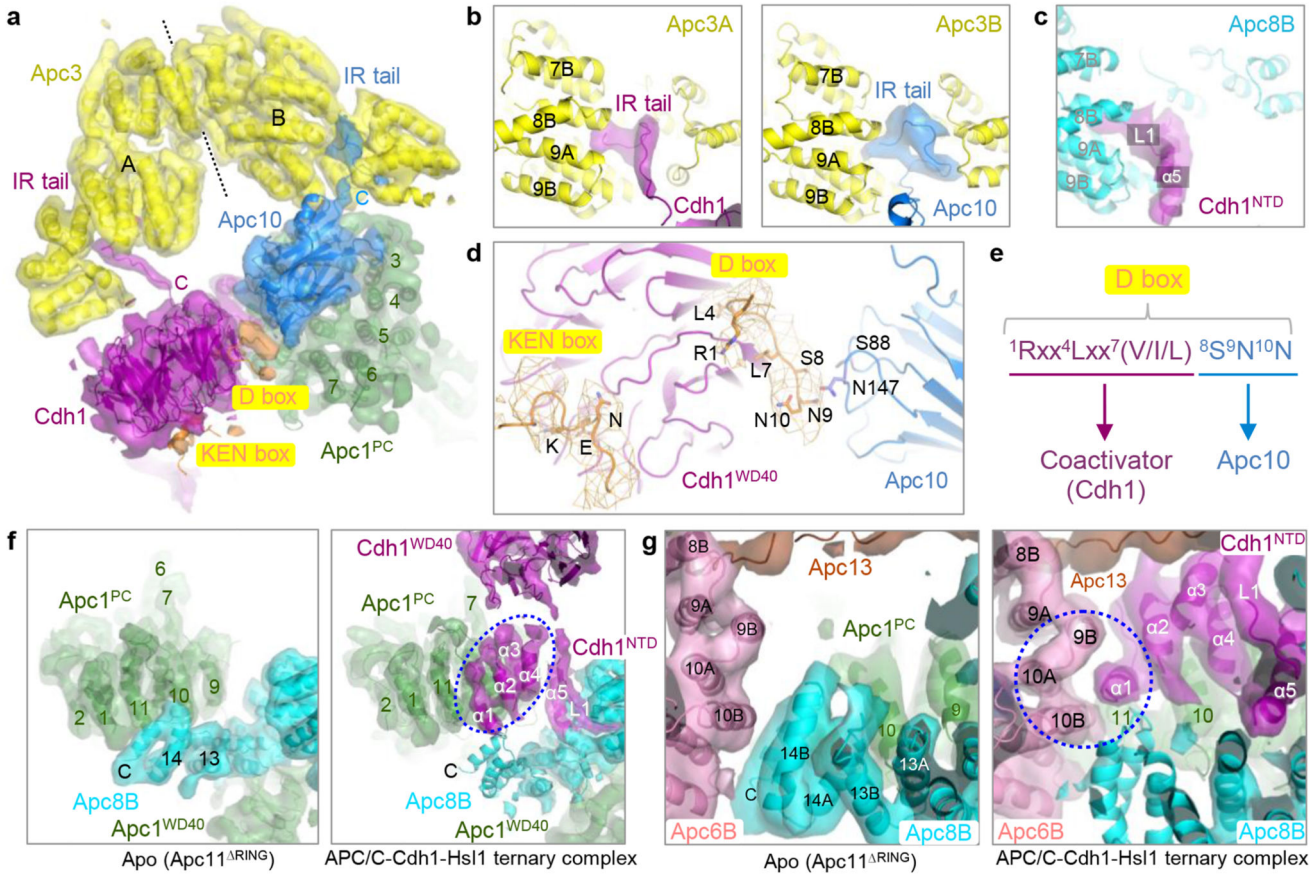

Figure 4. Mechanism of D box recognition by Cdh1 and Apc10 and interactions with APC/C subunits

(**a**) View showing IR tails of Cdh1 and Apc10 interacting with equivalent, symmetry-related sites on the Apc3 homo-dimer. (**b**) The IR tails of Cdh1 and Apc10 interact with equivalent TPR motifs 7 to 9 of symmetry-related subunits of the Apc3 homo-dimer. (**c**) Cdh1^{NTD} interacts with Apc8B, including TPR motifs equivalent to the IR tail-binding sites of Apc3. (**d**) EM density (mesh) at the KEN box and D box sites of Cdh1. EM density for the D box interacting with two conserved loops of Apc10 is visible. (**e**) D box interacts as a bi-partite degron with the D box co-receptor of Cdh1 and Apc10. Shown is a D box consensus sequence [26]. (**f**) Interaction of Cdh1^{NTD} with the Apc1^{PC} displaces Apc1^{PC} – Apc8 interactions. (**g**) Cdh1^{NTD} interactions with Apc6 (circled in right panel).

Europe PMC Funders Author Manuscripts

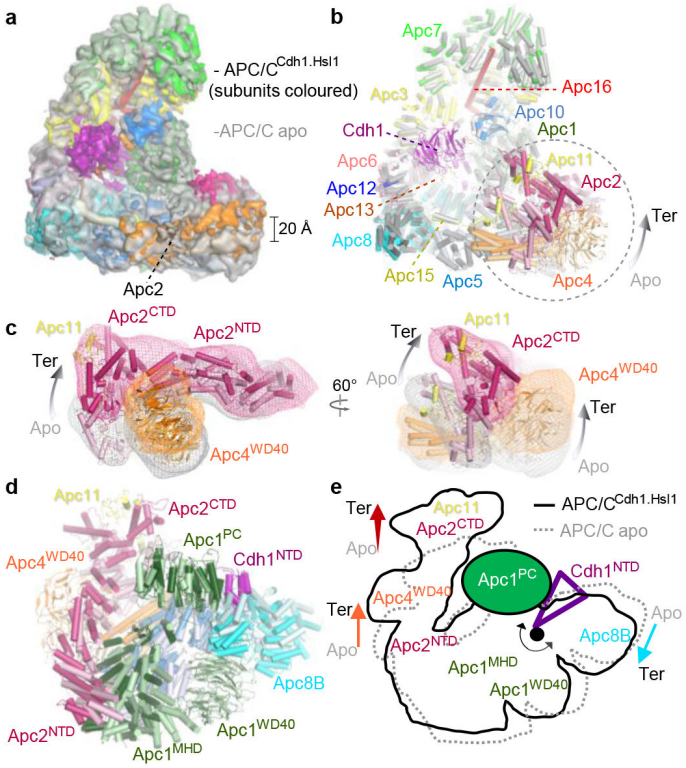

Figure 5. Conformational change of the APC/C induced by Cdh1^{NTD}

(**a**) Superimposition of ternary and apo APC/C maps. The ternary map is colour-coded according to the subunits assignments of Fig. 1. Apo map is in grey. (**b**) Superimposition of the apo and ternary coordinates. Apo coordinates are in grey except Apc2, Apc11 and Apc4 shown in a lighter shade relative to the ternary complex. (**c**) Two views showing the displacement of Apc2-Apc11 and Apc4^{WD40}. (**d**) View of rotation of the platform subunits on transition from apo to ternary states. Subunits of apo APC/C are shown in a lighter shade relative to the ternary complex. (**e**) Schematic of the platform displacement. Insertion of Cdh1^{NTD} (depicted as a wedge) between Apc1^{PC} and Apc8B causes platform rotation about the fixed Apc1^{PC} domain. This propagates a 20-Å shift to Apc2^{CTD}-Apc11.
The rotation axis is shown as a black circle.